Single- vs. Dual-Source Vapor Deposition of Inorganic Halide Perovskites: A Case Study of CsPbBr₃

Tomáš Musálek^{1,2}, Petr Liška^{1,2}, Amedeo Morsa³, Jon Ander Arregi², Pavel Klok¹, Matouš

Kratochvíl⁴, Dmitry Sergeev^{3,5}, Michael Müller³, Tomáš Šikola^{1,2}, Miroslav Kolíbal^{1,2,*}

¹Institute of Physical Engineering, Brno University of Technology, Technická 2, 616 69 Brno,

Czech Republic

²CEITEC BUT, Brno University of Technology, Purkyňova 123, 612 00 Brno, Czech

Republic

³Institute of Energy Materials and Devices, Structure and Properties of Materials (IMD-1),

Forschungszentrum Jülich, 52425 Jülich, Germany

⁴Materials Research Centre, Faculty of Chemistry, Brno University of Technology,

Purkyňova 118, 612 00 Brno, Czech Republic

⁵NETZSCH-Gerätebau GmbH, Selb, D-95100, Germany

* mail: kolibal.m@fme.vutbr.cz

Abstract

Inorganic halide perovskites have become attractive for many optoelectronic applications due

to their outstanding properties. While chemical synthesis techniques have been successful in

producing high-quality perovskite crystals, scaling up to wafer-scale thin films remains

challenging. Vapor deposition methods, particularly physical vapor deposition and chemical

vapor deposition, have emerged as potential solutions for large-scale thin film fabrication.

However, the control of phase purity during deposition remains problematic. Here, we

investigate single-source (CsPbBr₃) and dual-source (CsBr and PbBr₂) physical vapor

deposition techniques with the aim of achieving phase-pure CsPbBr₃ thin films. Utilizing

Knudsen Effusion Mass Spectrometry, we demonstrate that while the single-source CsPbBr₃

1

evaporation is partially congruent, it leads to compositional changes in the evaporant over time. The dual-source evaporation, with a precise control of the PbBr₂/CsBr flux ratio, can improve phase purity, particularly at elevated substrate temperatures at excess PbBr₂ conditions. Our results give direct evidence that the growth is CsBr-limited. Overall, our findings provide critical insights into the vapor phase deposition processes, highlighting the importance of evaporation conditions in achieving the desired inorganic perovskite stoichiometry and morphology.

I. Introduction

Inorganic halide perovskites have received tremendous and still increasing attention from the scientific community because of their excellent optoelectronic properties, which qualify them for use in solar cells, light-emitting diodes, ¹ X-ray detectors, and more. ² This rapid burst of scientific studies was fuelled mainly by chemical synthesis preparation techniques, which provide high-quality perovskite (nano)crystals at very low costs. ³ However, upscaling this approach to wafer-scale thin films poses a great challenge. Recently, vapor deposition techniques have come to focus; evaporation from a solid source under vacuum conditions is an established technology, e.g., in semiconductor lasers, allowing the preparation of thin films with atomic-scale precision. ⁴ Building on a large know-how from different material systems, deposition from a vapor phase has the potential to become a dominant technology for a large-scale deposition of inorganic halide perovskite thin films as well.

The perovskite preparation technique is vital to determine the relevant properties of the resultant thin film.⁵ Many experimental studies on vapor deposition of halide perovskites have been recently summarized by timely and important reviews.⁶⁻⁸ Importantly, if effusion cells are utilized, vapor deposition offers much better control of the evaporation fluxes, thus allowing to

engineer the grain size^{9,10} or the intermixing of different chalcogenides.¹¹ The efficacy of vapor deposition has soon been recognized and demonstrated by the deposition of the perovskite solar cells¹² and the perovskite light emitting diodes.^{13,14} However, many issues prevail. Deposition of CsPbBr₃ by evaporation of precursors of different composition results in thin films of CsPbBr₃ mixed with unreacted CsBr and PbBr₂ or other phases of a different stoichiometry. Hence, the phase-purity control is poor even for the most prominent inorganic halide perovskite, CsPbBr₃. Overall, the literature reviews give a clear picture of current know-how in the field: a comprehensive understanding of the processes involved in every stage of the growth (evaporation, transport, and growth) is lacking.⁶⁻⁸

The most prominent approaches to vacuum-based vapor deposition are chemical vapor deposition (CVD) and evaporation from Knudsen-like cells, the latter belonging to the family of physical vapor deposition (PVD) techniques. Usually, CVD relies on tubular quartz reactors, where, for instance, the precursor powders are placed at a certain position within a temperature gradient across the furnace. The vaporized precursors are dragged by a carrier gas toward the substrate, which is located at different positions within the tube furnace; here, the vapors condense into a thin layer. A sealed variant of CVD (without the carrier gas) is called the chemical vapor transport (CVT); here, the sample size is limited. Tubular quartz CVD and CVT reactors that utilize solid precursors are mostly single-use; after each growth run, the precursors need to be refilled. Only recently, experimental CVD setups for perovskite growth that do not require frequent precursor refilling were introduced. ^{15,16} In contrast to tubular quartz CVD, PVD techniques are typically housed in larger high-vacuum apparatuses, ⁸ where the Knudsen cells do not require refilling after every deposition, thus ideally providing stable and reproducible growth runs. However, typically in perovskites growth, this is difficult to achieve, as it is shown in this paper.

Most often, the precursors in Knudsen cells are located in resistively heated crucibles. Another possibility, specifically for organic-inorganic perovskites, is the pulsed laser deposition (PLD)¹⁷ or its variant, resonant infrared matrix-assisted pulsed laser evaporation (RIR-MAPLE).¹⁸ These technologies seem very promising but remain unexplored.

Regardless of the technology in use, the deposition of a multicomponent materials is done from individual precursors of each component placed separately in different heating zones¹⁹ or separate evaporation cells, ²⁰⁻²² as well as from a single precursor. ^{11,23,24} The former approach promises a good stoichiometry control of the resulting material via tuning the evaporation fluxes of each constituent (e.g. CsBr and PbBr₂). Certainly, most studies focused on finding the optimum evaporation flux ratio.²⁵⁻²⁷ With rare exceptions, ²⁸ depositing two constituents at 1:1 evaporation flux ratio does not lead to stoichiometry preservation of the deposit (CsBr+PbBr₂=CsPbBr₃). The on-surface growth is determined by kinetic processes, schematically illustrated in Fig. 1, that significantly alter the individual surface concentration of species involved.^{29,30} These processes are thermally activated and follow Bolzmann statistics. Typically, high diffusivity at the surface is a key factor for the deposited atoms and molecules to reach low-energy positions.³¹ If multicomponent materials are deposited, one ideally needs a high diffusivity and similar desorption rate of all constituents simultaneously,³² which is usually not the case (despite the fact that, for example, the CsPbBr₃ formation from gaseous CsBr and PbBr₂ is exothermic, -386 kJ/mol, 13 providing an additional thermal energy to deposited molecules). Such a situation is schematically illustrated in Fig.1, where imbalance in the surface fluxes of individual constituents arises due to the enhanced desorption of one of the species. Specifically, for halide perovskites, a proposed solution to this issue involves a sequential, separate evaporation of each component, one after another, followed by annealing of the entire multilayer stack.³³ However, post-growth annealing is another critical step that faces several kinetic restrictions. Perfect mixing is achieved only if the temperature is high

enough to promote interdiffusion while avoiding PbBr₂ desorption. An alternative approach could be the deposition of multiple layer sequences, but in principle, the difficulties associated with annealing persist.³⁴ Additionally, issues arise outside of vacuum conditions due to varying levels of humidity.³⁵

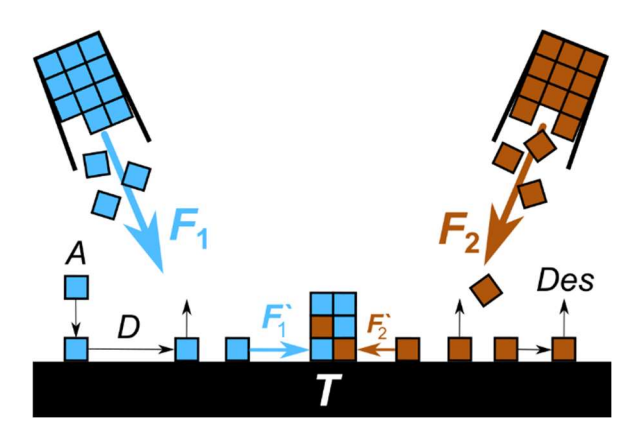


Fig. 1: Schematic illustration of the processes involved in multicomponent deposition. In this case, two evaporation sources (blue and brown) of different constituents (blue and brown bricks) are evaporated at the same evaporation rates F, i.e. $F_1 = F_2$. Nevertheless, the on-surface fluxes, $F_1 > F_2$, are not equal due to different kinetic rates of on-surface processes for each constituent (A – adsorption, D – diffusion, D – desorption). The kinetic rates are significantly dependent on sample temperature T. Hence, the growth may not result in stoichiometric product and the initial 1:1 ratio of the evaporation fluxes F_1 and F_2 is not preserved on the surface.

Hence, an important "turning knob" for optimizing the growth process and achieving the correct stoichiometry is the sample temperature T.²⁹ The numerous surface processes are difficult to precisely control by only two variables (sample temperature and precursor fluxes). Nevertheless, it is possible to built on previously established compound semiconductor deposition processes, utilizing self-limited kinetics of the growth system. This is the case, e.g., of GaAs, ³⁶ and SnSe, ³⁷ where the growth is Ga- and Sn-limited, respectively. The self-limiting conditions are achieved at elevated temperature under excess group V (or VI) precursor flux. High temperatures ensure that excess As (or Se) atoms are readily desorbed, leaving only those that form Ga-As (or Sn-Se) bonds and remain on the surface. Thus, an optimum stoichiometric

III-V crystal growth is achieved. Such an approach has not been studied for halide perovskites, as the knowledge of surface processes that occur during growth from multiple precursor sources is rather limited.

Alternatively, evaporation from a single source (i.e., CsPbBr₃) has the potential to simplify the phase-pure deposition, provided that the compound evaporates congruently. That means the composition of the vapor is reflecting that of the evaporant.^{38,39} This is possible if the precursor is in the form of a nanoscale powder or if the precursor pellet fragments into nanoscale parts and decomposes only after fragmentation.³⁹ The latter process has recently been documented to occur during the melting of CsPbBr₃.⁴⁰ However, the congruent evaporation of CsPbBr₃ has not yet been validated, despite speculations in the literature.²⁶ Understanding the single-source evaporation of CsPbBr₃ is complicated as different phases of the resulting perovskite layers are reported, being Cs or Pb rich.^{41,42} Post-growth alloying strategies have been employed to increase the purity of the CsPbBr₃ phase, ^{41,42,25} but this approach faces similar issues as the aforementioned annealing of multilayer stacks.^{34,35} An apparent solution is the deposition at elevated temperature. Although this increases complexity, at the same time it introduces possibility of tuning the resulting morphology, from polycrystalline layers at lower temperatures to nanowires at higher temperatures, ^{19,24} although contradictory results have been reported so far.¹¹

Here, we study single-source (CsPbBr₃) and dual-source (CsBr and PbBr₂) deposition strategies with the objective of depositing phase-pure CsPbBr₃. We analyze two critical phases of growth by separately analyzing the evaporation products using Knudsen Effusion Mass Spectrometry (KEMS) and the growth products at different sample temperatures by relevant analytical techniques. We show that the decomposition of CsPbBr₃ is partially congruent; however, the precursor composition changes during the evaporation. It is observed that this problem can be resolved to some extent by elevating the sample temperature, which enhances the phase purity

of the deposit by desorbing excess PbBr₂. Similarly, the dual-source evaporation yields a high-purity CsPbBr₃ evaporant at elevated sample temperatures, because growth is CsBr-limited. At lower sample temperatures, other phases, namely CsPb₂Br₅ and Cs₄PbBr₆, are detected on the samples, either pure or mixed with CsPbBr₃, CsBr, or PbBr₂.

II. Methods:

Perovskite CsPbBr₃ precursor synthesis: PbBr₂ powder (Sigma Aldrich, 99.999% purity) was dissolved in 48% aqueous HBr, and CsBr powder (Sigma Aldrich, 99.999% purity) was dissolved in H₂O. In both cases the molar ratio of the dissolved powders was 1:1. Next, the solutions are mixed, resulting in the precipitation of orange solid, which was suction filtered, washed with ethanol, and dried under vacuum. For co-evaporation experiments, pure PbBr₂ and CsBr powders were used.

Perovskite evaporation: All evaporation experiments were conducted within a high vacuum (HV) chamber, maintaining a base pressure of 1×10⁻⁸ mbar. The chamber was equipped with two custom-built resistively-heated effusion cells, both aligned at an incident angle of 30° relative to the substrate. During the operation, the pressure typically stabilized in the order of 10⁻⁷ mbar. The evaporators were operated at 450 °C for the evaporation of single-source CsPbBr₃, and in the range of 400-450 °C and 240-360 °C for the evaporation of CsBr and PbBr₂, respectively. The evaporation rates were calibrated by a quartz crystal microbalance and validated on room-temperature deposited layers by step-height measurement by atomic force microscopy. The sample holder was fitted with a calibrated pyrolytic boron nitride (pBN) heater to ensure a precise temperature control. Si(111) substrates were used in all the experiments.

X-ray diffraction (XRD): Structural analysis and phase identification of the deposited Cs-Pb-Br samples was performed via in-plane grazing incidence XRD (GIXRD) measurements and out-of-plane specular diffraction using a Rigaku Smartlab (9 kW) diffractometer with Cu-K α radiation (λ = 1.54 Å) and an incident parallel beam setting. A 5° in-plane Soller slit was utilized in both the incident and diffracted optics. For GIXRD, the X-ray source and the detector were set to a grazing angle (ω = 0.8°, 2 θ = 1.6°) and intensity profiles were acquired by scanning the 2 θ / χ angle, where the detector arm is laterally scanned in order to look for crystalline planes that are perpendicular to the sample surface. The grazing-incidence measurement geometry maximizes the signal arising from the thin film in comparison to that of the substrate. In specific cases, we have also utilized the out-of-plane diffraction geometry (specular diffraction) by performing symmetric θ -2 θ scans using a double-bounce Ge(022) monochromator, obtaining reflections from crystallographic planes parallel to the sample surface. Such a configuration allows scanning the 2 θ angle with better resolution, which is necessary for discriminating between the orthorhombic and cubic CsPbBr₃ phases. The recorded peaks were compared to crystallographic databases (see Fig. S1).

Scanning electron microscopy (SEM) was performed using ThermoFisher Verios 450L and FEI Versa microscopes.

X-Ray Photoelectron Spectroscopy (XPS): compositional analysis was performed using a Kratos Axis Supra XPS instrument utilizing the monochromated Al K α radiation (1486.6 eV) and a hemispherical analyzer set in a high magnification mode with a pass energy of 20 eV. The electron emission angle was set along the normal to the surface. All the spectra were acquired with an energy step of 0.05 eV. The perovskite phase analysis, presented in the Supplementary Material, was performed without shifting the spectra. Only to clearly present the Pb⁰ component after prolonged X-Ray irradiation, we have shifted the spectra shown in Fig. 6 with respect to the Pb²⁺ component at 138.75 eV.⁴³ The intensity and fluence of the X-Ray source were determined according to Ref. ⁴⁴.

Photoluminescence and Raman spectroscopy analysis: spectra were obtained using a Witec Alpha 300R confocal microscope set-up with a built-in spectral camera and continuous wave laser illumination. The wavelength of the laser light used for excitation was 532 nm and the optical power of the laser varied from 0.5 mW to 10 mW. The spectra were normalized with respect to the intensity of the Si Raman peak (520 cm⁻¹). All the measurements were done using an objective lens with 100× magnification, 0.3 mm working distance and 0.9 numerical aperture. The diffraction grid settings for photoluminescence measurements and for the detailed Raman spectra observations were 600 g/mm and 1200 g/mm, respectively.

For time-resolved photoluminescence (TRPL) measurements, free space optics was used. The sample was placed into a Ø50 mm Thorlabs integration sphere with three SM05-threaded input ports and one SM05-threaded output port. The integration sphere has a reflectance greater than 94% over the wavelength range of 250 nm to 2500 nm. Through one SM05-threaded input port, excitation light from a pulsed laser diode (PIL 040-FS) with a 407 nm wavelength, 100 ps pulse width, 1.46 mW optical power, and 10 MHz repetition rate, was directed onto the sample placed inside the integration sphere. The TRPL was collected through the SM05-threaded output port and directed to an avalanche photodiode (SPCM-AQRH-64, Excelitas Technologies). The measured PL intensities were fitted with a single-exponential function as follows:

$$I(t) = I_0 exp\left(-\frac{t}{\tau_1}\right) \tag{1}$$

where I(t) is the PL intensity at time t, whereas I_0 and τ_1 are the amplitude and the lifetime of the charge transfer process.

For photoluminescence quantum yield measurements (PLQY), the same set-up as for TRPL was used with some modifications. The excitation pulsed laser light, with 407 nm wavelength, was operated at an optical power of 0.84 mW and a repetition rate of 20 MHz. The signal was collected through the SM05-threaded output port and directed to a Shamrock spectrograph 303i

equipped with an iDus 420 CCD camera from Oxford Instruments, a diffraction grating of 150 g/mm, input slit size of 10 μ m, and integration time 10 s. The PLQY was obtained and calculated as

$$\eta_{\text{PLQY}} = \frac{A_{\text{PL}}}{A_{\text{inc.}} - A_{\text{scat.}}} \cdot 100,\tag{2}$$

where A_{PL} is the area under the photoluminescence curve, $A_{inc.}$ is the area under the reflectance curve of the bare substrate and $A_{scat.}$ is the area under the reflectance curve of the substrate covered by the perovskite thin film.

Knudsen effusion mass spectrometry experiments were conducted using a FINNIGAN MAT 271 spectrometer at Forschungszentrum Jülich. Prior to sample introduction, the Knudsen cells were preconditioned by heating at 1000 °C for 12 hours to remove impurities. For each measurement, approximately 40 mg of sample powder were loaded into the cell. Ionization was performed using an electron beam generated by a tungsten cathode, operating at an energy of 60–70 eV and an emission current of 0.47 mA. Two types of measurement series were carried out: isothermal measurements, where vapor species were analyzed at a constant temperature over time, and polythermal measurements, which were taken at different temperature intervals. Full experimental details are provided in the Supplementary Material.

III. Results

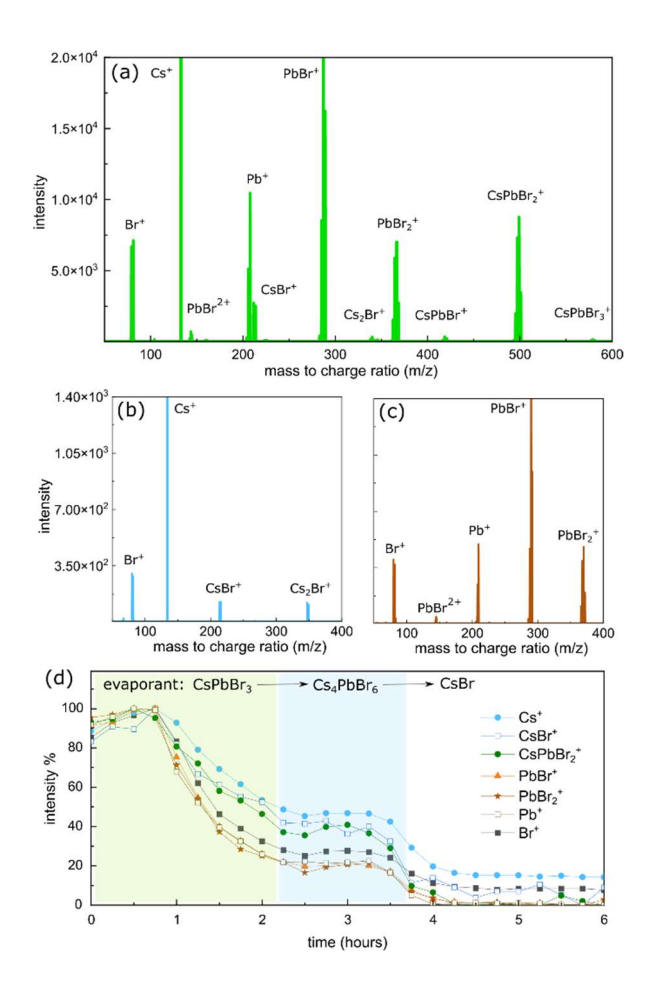


Fig. 2: KEMS results: mass spectra of (a) CsPbBr₃ pellet held at 450 °C, (b) CsBr powder at 450 °C, (c) PbBr₂ powder at 300 °C. (d) Isothermal evaporation of the CsPbBr₃ evaporant at 450 °C, the most relevant components monitored in time (only selected components are shown for clarity; more data are in Supplementary Material, Fig. S3). The PbBr-related components are depleted faster (faster decrease in the graph for PbBr⁺, PbBr₂⁺, Pb⁺ and Br⁺) and at a certain moment a phase change to Cs₄PbBr₆ occurs. When all PbBr₂ evaporates, only CsBr remains.

The species evaporated from the source materials are the building blocks for further perovskite phase formation on the substrate. We have utilized KEMS to identify the evaporated species from the single-source (CsPbBr₃ pellet) as well as dual-source precursor(s) (CsBr and PbBr₂ powders). Fig. 2 shows a mass spectrum recorded for each of these source materials heated to the temperatures further used in this study: CsPbBr₃ at 450 °C (Fig. 2a), CsBr at 450 °C (Fig.

2b), and PbBr₂ at 300 °C (Fig. 2c). As expected, the CsPbBr₃ KEMS spectrum contains ions that do not appear in the spectra of CsBr or PbBr₂ alone, including CsPbBr₂⁺ (493-503 m/z) which results from the fragmentation of CsPbBr3 molecules after ionization. Although the fragmentation is very efficient (compare the intensity of CsPbBr₂⁺ and CsPbBr₃⁺ peaks in Fig. 2a), the presence of these components in the mass spectrum is indisputable proof that a congruent evaporation of CsPbBr₃ occurs as well. However, the congruent evaporation is only a partial, although major process. This is documented by the existence of Cs₂Br⁺, which can hardly originate from the CsPbBr₃ molecular clusters alone. Its presence indicates that (CsBr)_x clusters evaporate as well $(x\geq 2)$. Therefore, in addition to the congruent evaporation, the precursor in the crucible partially decomposes into CsBr and PbBr₂, and these components evaporate (at different rates, see below) simultaneously with the congruently evaporated CsPbBr₃ (see Fig. 2d). An extended analysis of KEMS data, including detailed temperature dependencies that further support these conclusions, is shown in the Supplementary Material (Fig. S4, S5 and S6). The equilibrium vapor pressure of PbBr₂ is higher as compared to that of CsBr;^{45,46} therefore, if kept at the same temperature, PbBr₂ evaporates faster (compare the absolute ion currents in Fig. 2b,c). This fact is also documented in Fig. 2d, where the isothermal evaporation of CsPbBr3 is monitored over time. The intensity of PbBr2-related ions decreases faster compared to CsBr-ones. Therefore, the composition of the evaporant in the crucible gradually changes over time towards the Cs-rich phase. Consistent with the CsBr-PbBr₂ phase diagram, ²⁵ when a certain stoichiometry is reached (ratio 4:1), the phase change of the evaporant to Cs₄PbBr₆ occurs. This phase change is accompanied by different evaporation rates, followed by a rapid loss of PbBr-related components (clearly distinguishable in Fig. 2d). Then, only CsBr is left within the crucible. Thus, KEMS measurements explain the previous experimental findings reporting different evaporant compositions after growth runs. ^{26,41}

Congruent evaporation typically occurs in nanocrystalline evaporants because the heat is delivered abruptly to the entire nanocrystal, leading to a rapid decomposition and evaporation.³⁹ Therefore, the preparation method is expected to be important. Nevertheless, we have found that different forms of the evaporant produce very similar results (see Supplementary Material, Fig. S4). Additionally, for evaporant temperatures between 400 °C and 450 °C, the vapor composition (ratios between components) is stable with the temperature (see Fig. S6). Thus, if operated before the phase change to Cs₄PbBr₆ and considering that vapor pressure depends on temperature, the single-source CsPbBr₃ evaporation also allows control of the deposition rate by adjusting the evaporant temperature.

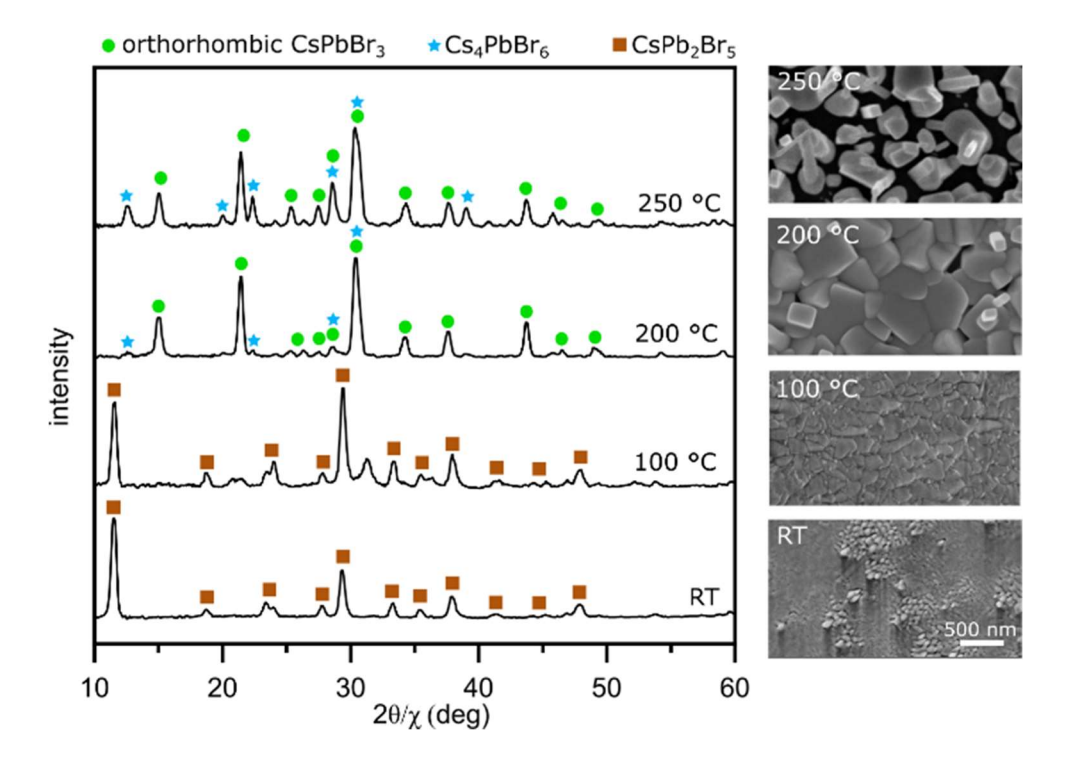


Fig. 3: Analysis of single-source (CsPbBr₃, 450 °C, evaporation rate was 15 nm/min) deposited perovskite layers (30 minutes deposition) at different substrate temperatures (RT, 100 °C, 200 °C, 250 °C). Peaks in XRD spectra are marked by symbols relevant for each phase: orthorhombic CsPbBr₃ (●), CsPb₂Br₅ (■) and Cs₄PbBr₆ (*) (see Fig. S1 for the full spectra and detailed peak assignments). Representative SEM images of each sample are shown on the right.

Next, we show that it is possible to substantially tune the stoichiometry of the deposited layers by controlling the substrate temperature, without requiring extensive flux control. First, in Fig. 3 we show the XRD and SEM analyses of layers deposited from a single-source evaporant (CsPbBr₃) at substrate temperatures ranging from room temperature (RT) to 250 °C. All growth runs were performed using a fresh evaporant at 450 °C to avoid changes in flux compositions due to phase changes in the evaporant (see Fig. 2d). We observe that both the RT and 100 °C depositions yield a compact layer of CsPb₂Br₅ (see Fig. 3). Upon increasing the substrate temperature, the grain size of the deposit slightly increases, while the nominal layer thickness corresponds to the deposition rate (470 nm). Conversely, we find that the morphology of the layer deposited at 200 °C is strikingly different. The individual grains possess a nearly cubic shape and, occasionally, nanowires of a rectangular cross-section (up to 300 nm size) and a maximum length of 2 µm are protruding the polycrystalline layer. We argue that the appearance of the layer is clearly related to the phase change. At 200 °C, an orthorhombic CsPbBr₃ phase is identified in the XRD spectra (see left panel in Fig. 3 and Fig. S7 in SI for crystal phase identification) with only a very minor presence of Cs₄PbBr₆. At a higher sample temperature (250 °C), the fraction of Cs₄PbBr₆ slightly increases. At even higher temperature (300 °C, not shown), no layer is formed, as all deposited material is desorbed. Further analyses by XPS and Raman spectroscopy (see Supplementary Material, Figs. S8 and S9) support the phases identified by XRD.

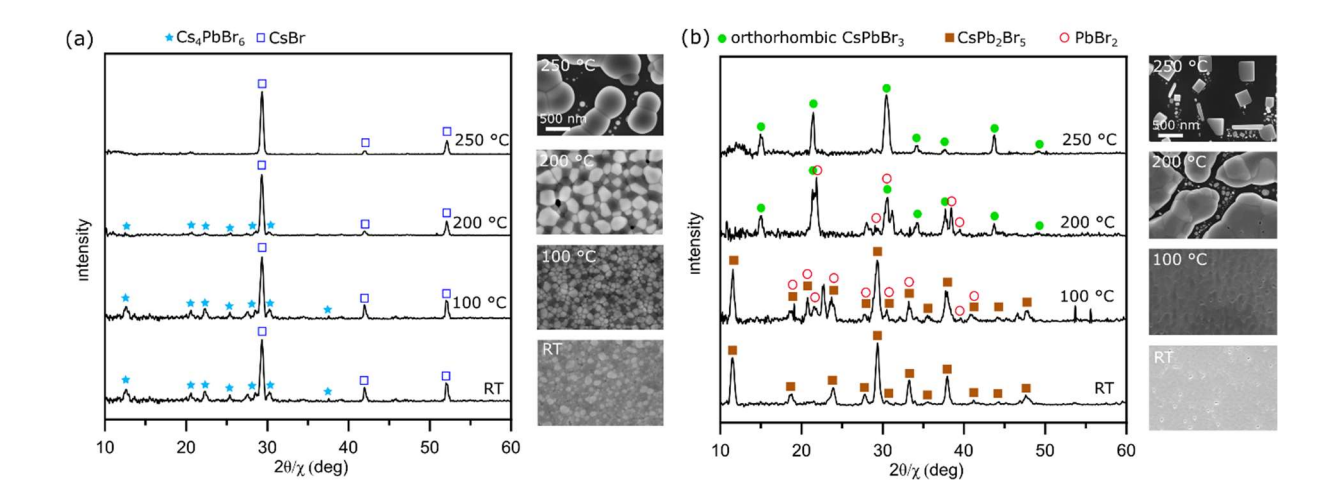


Fig. 4: Analysis of dual-source (CsBr and PbBr₂) deposited perovskite layers at different sample temperatures (RT, 100 °C, 200 °C, 250 °C) and flux ratios. In (a) the XRD and SEM analysis of the layers deposited with a PbBr₂/CsBr flux ratio of 1:5 is shown. The evaporator temperatures were 240 °C and 450 °C, providing absolute fluxes of 0.8 nm/min and 4 nm/min for PbBr₂ and CsBr, respectively. In (b), the same analysis is made for a PbBr₂/CsBr flux ratio of 4:1. The evaporator temperatures were 300 °C and 400 °C, providing absolute fluxes of 8 nm/min and 2 nm/min for PbBr₂ and CsBr, respectively. Peaks in XRD spectra are marked by symbols relevant for each phase: orthorhombic CsPbBr₃ (●), CsPb₂Br₅ (■), Cs₄PbBr₆ (*), CsBr (□) and PbBr₂ (○) (see Fig. S1 for the full spectra and detailed peak assignments).

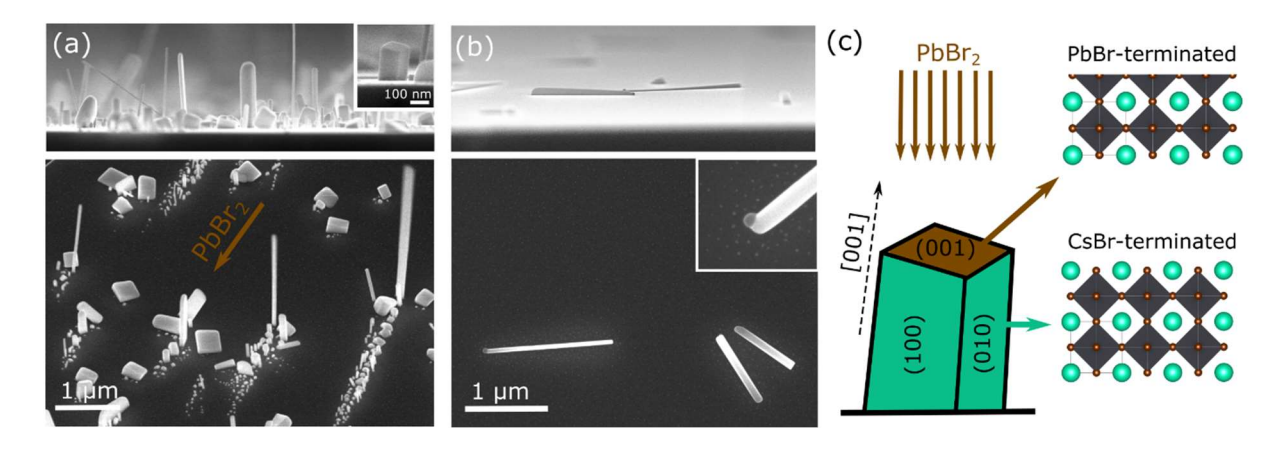


Fig. 5: CsPbBr₃ nanowires observed when higher substrate temperatures and PbBr₂ flux (dual source deposition) were used. In (a), a detailed SEM inspection of the sample grown at 250 °C (same as in Fig. 4b, PbBr₂/CsBr flux ratio of 4:1) is shown, with the side view in the top row, and a tilted (45°) view in the bottom row. At 250 °C, out-of-plane CsPbBr₃ nanowires are formed, with cuboid CsPbBr₃ crystals mostly within the shade of nanowires in the direction of the PbBr₂ beam (the beam direction is marked by an arrow, the sample was not rotated during the evaporation). A SEM image of a slightly elongated

cuboid crystal, with a clearly visible square top facet, which is identical to the nanowire cross-section is shown in the inset. (b) The sample grown at 300 °C using a very high PbBr₂/CsBr flux ratio of 25:1, where exclusively in-plane oriented CsPbBr₃ nanowires are formed. The evaporation temperatures were 360 °C and 400 °C, providing absolute fluxes of 50 nm/min and 2 nm/min for PbBr₂ and CsBr, respectively. The inset shows a detail of a nanowire tip with a nanoparticle, typical for vapor-solid-solid growth. (c) The schematic illustration shows the proposed model for anisotropic growth, including the side views of Cs-Br- and Pb-Br-terminated facets.

The dual-source deposition (simultaneous independent evaporation of CsBr and PbBr₂) allows tuning the PbBr₂/CsBr flux ratio. Fig. 4a shows XRD and SEM analysis of layers deposited at sample temperatures ranging from RT to 250 °C when the flux ratio is smaller than 1 (in this case, the PbBr₂/CsBr flux ratio was 1:5). All the layers are composed mostly of CsBr. Only for lower sample temperatures (RT and 100 °C), a certain fraction of Cs₄PbBr₆ is detected. As expected, the grain size increases with temperature. At 250 °C, the layer is partially decomposed and roughened (similarly to the single-source deposition). When the PbBr₂/CsBr flux ratio is changed to 4:1 (Fig. 4b), the XRD analysis of perovskite phases resemble those of the singlesource evaporation. The compact layer of CsPb₂Br₅ is deposited at low temperatures (RT and 100 °C), while at higher temperatures, orthorhombic CsPbBr₃ is formed. However, in contrast to the single-source evaporation, there are several noticeable differences. Firstly, below 250 °C, the temperature is not high enough to evaporate excess PbBr₂, as deduced from the PbBr₂ signatures in the XRD. Importantly, pure orthorhombic CsPbBr₃ is formed at 250 °C (other phases were not detectable by XRD). At this temperature, the Cs₄PbBr₆ present in samples prepared by the single-source evaporation is absent. CsPbBr₃ deposited at 250 °C forms welldefined cuboid crystals as well as nanowires.

We have inspected the sample grown at 250 °C in more detail (see Fig. 5a). The nanowires on the sample were all out-of-plane, no in-plane nanowires were observed. All the nanowires have a square cross section (see detail in Fig. 5a). Interestingly, cuboid crystals on the sample

predominantly form near nanowires, appearing almost exclusively in their shadow along the direction of the PbBr₂ flux. The largest difference between the single- and dual-source evaporation is that using the latter approach the growth of CsPbBr₃ is possible also at temperatures above 250 °C. In order to do so, the PbBr₂/CsBr ratio has to be much higher compared to the one achievable by the single-source deposition. Fig. 5b additionally shows that at 300 °C and under a very high PbBr₂ flux (PbBr₂/CsBr flux ratio of 25:1), only small crystallites and relatively long CsPbBr₃ nanowires are present on the surface. Interestingly, in contrast to the deposition at 250 °C, all the nanowires grow in-plane, along the substrate surface. In many cases, a small droplet is visible at the nanowire end (see the inset in the bottom panel of Fig. 5b), and the nanowires are frequently tapered. XRD revealed that both out-of-plane and in-plane oriented nanowires exhibit orthorhombic CsPbBr₃ structure (Fig. S7).

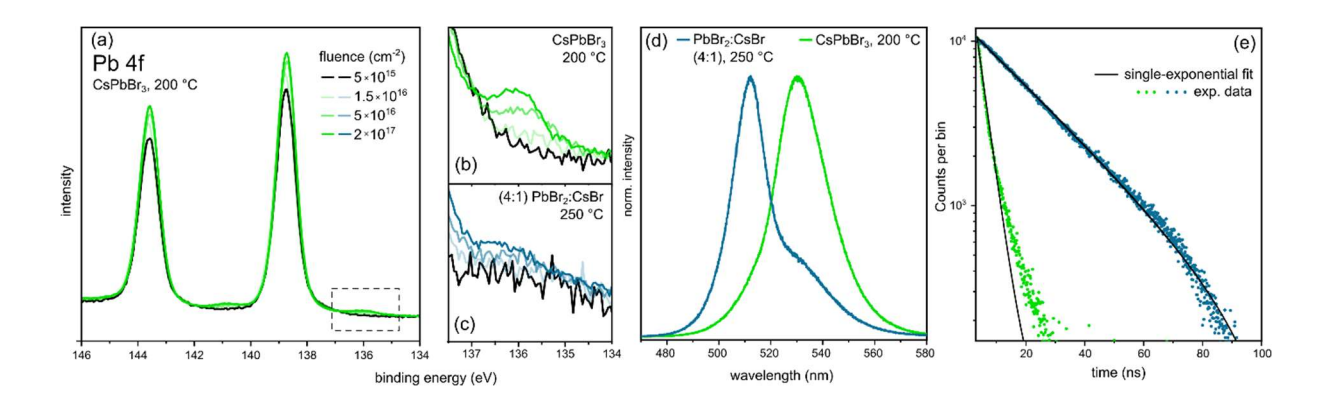


Fig. 6: Comparison of optoelectronic properties of CsPbBr₃ prepared by different approaches (dual source, PbBr₂+CsBr, 4:1, at 250 °C and single source, CsPbBr₃, at 200 °C). Panel (a) shows the X-ray-induced damage evolution of the single-source deposited sample, documented by XPS spectra (in the Pb 4f region) after exposure to 1486 eV X-Rays with an increasing fluence. A reduction of higher valence states of Pb to metallic Pb⁰ is documented by the appearance of a component at 136 eV, which is shown in detail in (b). The same spectral detail is shown in (c) for the CsPbBr₃ sample grown by dual-source deposition after exposure to the same X-Ray fluences. PL spectra and TRPL measurements of the two samples are shown in (d) and (e), respectively.

We have already demonstrated via XRD that dual-source deposition at sample temperatures above 200 °C produces better deposits in terms of phase purity. To support this conclusion with additional techniques, Fig. 6 illustrates the effects of X-Ray exposure (Fig. 6a-c), photoluminescence (PL, Fig. 6d) and time-resolved photoluminescence (TRPL, Fig. 6e) on the single-source deposited layer at 200 °C and the dual-source deposited samples (4:1 PbBr₂:CsBr ratio) at 250 °C (refer to Fig. 3 and 4b for XRD and SEM images). The degradation of halide perovskites under UV and X-Ray radiation is a well-known effect.⁴⁷ Formation of metallic Pb after the exposure to high-energy photons has been associated with PL quenching; subsequently, halide interstitials induce deep-level traps.⁴⁷ The former process is detectable through the emergence of a Pb⁰ component (metallic Pb) in the XPS spectrum. The series of XPS measurements under continuous X-Ray irradiation (1486 eV) shown in Fig. 6c indicates that the sample prepared by dual-source deposition exhibits negligible Pb⁰ formation, in contrast to single-source-deposited sample (Fig. 6b) where degradation is evident. It is worth noting, however, that the resistance of both samples to degradation under high-energy photon illumination is significantly greater when compared to samples composed of other perovskite phases (see Fig. S10). Deposits prepared using both deposition methods exhibit intense PL with peak maxima at positions characteristic of CsPbBr₃ (Fig. 6d).⁴⁸ The blueshift observed in the dual-source-deposited sample is attributed to quantum confinement effects in the nanowires and nanocubes present on the sample (see SEM images in Fig. 4b). 48 Time-resolved PL analysis reveals a single-exponential decay profile for the dual-source-deposited sample, whereas the single-source-deposited sample deviates from this behavior. The much longer exciton lifetimes observed in the dual-source-deposited sample (τ_1 =24.8 ns) are supported by PL quantum yield measurements, which reach 86%, a significantly higher value compared to the single-sourcedeposited sample (13%, τ_1 =3.4 ns).

IV. Discussion

Comparing the results of single-source and dual-source deposition leads to the following conclusions. At low deposition temperatures, our results agree with those reported by previous studies, 41,42 that is, both deposition approaches result in the CsPb₂Br₅ phase, occasionally mixed with CsPbBr₃. In order to grow the pure CsPbBr₃ phase, one needs to raise the sample temperature. The KEMS data, together with the analyses shown in Fig. 3 and Fig. 4, allow us to explain the mechanism behind. An elevated sample temperature results in desorption of excess PbBr₂ from the sample surface. The desorption of PbBr₂ prevents the formation of the CsPb₂Br₅ phase at temperatures above 100 °C. Instead, at elevated sample temperatures the growth rate becomes limited by the CsBr flux. This makes the CsPbBr₃ growth mechanism on surfaces very similar to that of III-V semiconductor formation via molecular beam epitaxy: in excess of group V species, the growth is controlled by the group III element. Here, the large flux of PbBr₂ allows the stoichiometric formation of CsPbBr₃, while the elevated sample temperature ensures the desorption of excess PbBr₂. This is valid for both the single-source and dual-source (with PbBr₂/CsBr flux ratios >1) depositions. The PbBr₂/CsBr flux ratio should be large; otherwise, the desorption of PbBr₂ could be so fast that growth of CsPbBr₃ can become PbBr₂-limited. This is the case of single-source deposition at 250 °C (Fig. 3). In such a case, the lack of PbBr₂ (and, hence, excess of CsBr) results in a partial formation of Cs₄PbBr₆. The desorption of PbBr2 is a temperature-activated process, but the loss of PbBr2 at high temperatures can be compensated by a very large PbBr₂ flux. This is achievable only through dual-source deposition enabling the growth of CsPbBr₃ at sample temperatures exceeding 250 °C with very high purity, as demonstrated in Fig. 6. Notably, high-temperature deposition ensures the desorption of any unreacted PbBr₂, efficiently eliminating PbBr₂ residues from the layer. Consequently, high-temperature-deposited layers exhibit higher photoluminescence quantum yield and longer exciton lifetimes. As shown in Figs. 4 and 5, increasing the sample

temperature and providing a high PbBr₂ flux cause the morphology of the CsPbBr₃ deposit to rapidly change from a fairly compact layer to nanowires. The appearance of nanowires during the vapor phase deposition of inorganic perovskites at elevated temperatures has been observed previously.^{19,24,49} This morphology change is still unexplored, despite attempts to explain it by temperature-dependent changes in the crystal structure.¹¹ Here, we observe two different cases. At the highest sample temperature of 300 °C inspected in this study (which is still below the liquidus line of the CsBr-PbBr₂ phase diagram), Cs-Pb-Br alloy nanoparticles are formed that further collect the deposited species, facilitating one-dimensional growth via vapor-solid-solid (VSS) mechanism.⁵⁰ The appearance of nanoparticles at the tip of the nanowires is a typical signature of VSS growth. The in-plane nanowire geometry reached at this deposition temperature results from a nanoparticle movement on the surface during growth.⁵¹ The nanoparticles shrink in time (and, potentially, fully diminish after some time), which is reflected in the tapered shape of the in-plane nanowires (Fig. 5b, side view).

At the slightly lower sample temperature of 250 °C, but still under high PbBr₂ flux, the out-of plane nanowires do not exhibit any nanoparticle at their tip. As the nanowire cross-section does not change along their axis, the absence of the droplet cannot be explained by its evaporation during growth. There is obviously another growth mechanism in play. We propose that the asymmetry promoting one-dimensional growth in the system is the distinct surface termination of CsPbBr₃ facets. Cuboid CsPbBr₃ crystals, as is the case here (Fig. 3), commonly exhibit (100) facets.¹⁹ These facets are crystallographically identical, and under common growth conditions they are Cs-Br terminated due to the lowest surface free energy of this termination.⁵²⁻⁵⁴ We hypothesize that, at PbBr₂-rich conditions, the facet that is most directly exposed to the incident flux transiently converts into a Pb-Br terminated one. Such a facet immediately develops to the fastest growing one due to an increase in the surface free energy.⁵² As a result, cuboid crystals elongate along the [100] direction (Fig. 5c) and form nanowires with a square

cross-section, observed experimentally (Fig. 5a). The elevated growth temperatures promote the relevant kinetic processes (mostly surface diffusion), further accentuating the anisotropy of the growth.

For many device applications, phase-pure, continuous CsPbBr₃ layers are essential. Our data indicate a sample-temperature-dependent trade-off between phase purity and the continuity of vapor-deposited perovskite layers. The morphology of these layers can be further manipulated through various means. Polycrystalline layers, such as those prepared in this study, are commonly formed during the vapor deposition of perovskites.⁵⁵ The compactness of polycrystalline films improves with increased nucleation density,⁵⁶ which is critically influenced by the D/F ratio.³⁰ At low D/F ratios, the higher concentration of surface species increases the likelihood of stable nuclei formation, resulting in more compact films.⁵⁶ SEM images in Fig. 3 and Fig. 4b clearly illustrate this behavior: at constant flux F, low-temperature depositions (corresponding to low D/F ratios) result in more continuous films, whereas highertemperature depositions (with higher D/F ratios) lead to predominantly isolated grains and nanowires. Therefore, phase-pure compact films can potentially be grown at elevated temperatures if the total flux F is significantly increased. Additional strategies to manipulate the growth mode include the appropriate choice of substrate (e.g., enabling epitaxial monocrystalline growth,)⁵⁷ or the use of surfactants.³⁰ The former approach builds on the fact that diffusion is strongly strain-dependent, allowing the D/F ratio to be adjusted through substrate selection. The latter technique, widely used in homoepitaxy of metals, 30 has yet to be explored for the growth of inorganic perovskites. Both approaches merit further detailed investigation.

Conclusions

In summary, we have demonstrated how differences in the vapor pressures of CsBr and PbBr₂ affect the vapor phase growth from both single- (CsPbBr₃) and dual-sources (CsBr and PbBr₂).

Under an excess PbBr₂ flux, the growth of CsPbBr₃ is CsBr-limited. Hence, if growth is conducted at certain elevated sample temperatures, this mechanism allows full control of the growth rate by the CsBr flux in case of the dual-source deposition. Similarly, it allows the deposition of the pure CsPbBr₃ phase. Our study shows that both single- and dual-source depositions of inorganic perovskites may result in layers with a prevailing CsPbBr₃ phase if appropriately controlled. The single-source deposition, however, requires caution; longer operation results in a phase change of the evaporant and related flux variations. Additionally, the dual-source deposition is more flexible, because it allows tuning the fluxes of each component independently. The ability to independently increase PbBr₂ flux is critical for phase-pure deposition of CsPbBr₃, as phase purity improves with sample temperature during deposition, provided that sufficient PbBr₂ flux is supplied. This has been demonstrated through XRD and PL measurements. Flux variations broaden the variety of CsPbBr₃ morphologies, ranging from cubic nanoparticles to nanowires. We have proposed a nanowire formation mechanism specific for CsPbBr₃ that explains the nanowire growth at high temperatures via changes in the surface-termination of the top facet under an excessive PbBr₂ flux.

Supplementary Material

Reference XRD data; description of the Knudsen Effusion Mass Spectrometer; additional KEMS data; additional XRD analysis; XPS analysis of the deposits; Raman spectrum of the CsPb₂Br₅ phase; additional references.

Acknowledgements

This article is partially based upon work from COST Action OPERA – European Network for Innovative and Advanced Epitaxy – CA20116, supported by COST (European Cooperation in Science and Technology, www.cost.eu). CzechNanoLab project LM2023051 funded by MEYS CR is gratefully acknowledged for the financial support of the measurements at CEITEC Nano

Research Infrastructure. This work was supported by the project Quantum materials for applications in sustainable technologies (QM4ST), funded as project No. CZ.02.01.01/00/22_008/0004572 by OP JAK, call Excellent Research, and the authors also acknowledge funding by Specific Research of BUT FCH/FSI-J-24-8514. We thank Martin Kovařík for AFM analysis of the layers.

Conflict of Interest Statement: The authors have no conflicts to disclose.

References

¹ Y. Zeng, Z. Dai, H. Liu, X. Zhang, D. Lin, H. Li, X. Pan, J. Wang, J. Du, F. Fan, Y. Zhang, S. Yu, H. Shen, and J. Luo, *Nat. Photonics* 17, 561 (2023). https://doi.org/10.1038/s41566-023-01177-1

- ² A. Rao, M. Shin, Y. Lee, H. Kang, J. Han, M. Kim, S. Jo, J. H. Kim, and S. H. Cho, *Nano Lett.* 24, 7717 (2024). https://doi.org/10.1021/acs.nanolett.3c04455
- ³ L. Protesescu, S. Yakunin, M. I. Bodnarchuk, F. Krieg, R. Caputo, C. H. Hendon, R. X. Yang, A. Walsh, and M. V. Kovalenko, *Nano Lett.* 15, 3692 (2015). https://doi.org/10.1021/nl5048779
- ⁴ B. Schwarz, P. Reininger, H. Detz, T. Zederbauer, A. M. Andrews, S. Kalchmair, W. Schrenk, O. Baumgartner, H. Kosina, and G. Strasser, *Appl. Phys. Lett.* 101, 191109 (2012). https://doi.org/10.1063/1.4767128
- ⁵ P. Zeng, Y. Wang, Q. Zhang, Y. Yang, J. Gong, G. Feng, and M. Liu, *J. Phys. Chem. Lett.* 14, 4638 (2023). https://doi.org/10.1021/acs.jpclett.3c00501
- ⁶ T. Soto-Montero, W. Soltanpoor, and M. Morales-Masis, *APL Mater.* 8, 111108 (2020). https://doi.org/10.1063/5.0027573

- ⁷ S. Bonomi and L. Malavasi, *J. Vac. Sci. Technol. A* 38, 063407 (2020). https://doi.org/10.1116/6.0000568
- ⁸ Q. Guesnay, F. Sahli, C. Ballif, and Q. Jeangros, *APL Mater.* 9, 100901 (2021). https://doi.org/10.1063/5.0060642
- ⁹ M. Shin, H. S. Lee, Y. C. Sim, Y. H. Cho, K. C. Choi, and B. Shin, *ACS Appl. Mater. Interfaces* 12, 1944 (2020). https://doi.org/10.1021/acsami.9b20094
- ¹⁰ I. J. Cleveland, M. N. Tran, A. Dey, and E. S. Aydil, *J. Vac. Sci. Technol. A* 39, 043403 (2021). https://doi.org/10.1116/6.0000875
- ¹¹ H. Zhou, S. Yuan, X. Wang, T. Xu, X. Wang, H. Li, W. Zheng, P. Fan, Y. Li, L. Sun, and A. Pan, *ACS Nano* 11, 1189 (2017). https://doi.org/10.1021/acsnano.6b07374
- ¹² M. Liu, M. B. Johnston, and H. J. Snaith, *Nature* 501, 395 (2013).
 https://doi.org/10.1038/nature12509
- ¹³ J. Li, P. Du, Q. Guo, L. Sun, Z. Shen, J. Zhu, C. Dong, L. Wang, X. Zhang, L. Li, and C. Yang, *Nat. Photonics* 17, 435 (2023). https://doi.org/10.1038/s41566-023-01177-1
- ¹⁴ Y. Hu, Q. Wang, Y. L. Shi, M. Li, L. Zhang, Z. K. Wang, and L. S. Liao, *J. Mater. Chem. C* 5, 8144 (2017). https://doi.org/10.1039/C7TC02477K
- ¹⁵C. P. Clark, B. Voigt, E. S. Aydil, and R. J. Holmes, *Sustainable Energy Fuels* 3, 2447 (2019). https://doi.org/10.1039/C9SE00200F
- ¹⁶ S. Sanders, D. Stümmler, P. Pfeiffer, N. Ackermann, G. Simkus, M. Heuken, P. K. Baumann,
 A. Vescan, and H. Kalisch, *Sci. Rep.* 9, 9774 (2019). https://doi.org/10.1038/s41598-019-46199-4

- ¹⁷ U. Bansode, R. Naphade, O. Game, S. Agarkar, and S. Ogale, *J. Phys. Chem. C* 119, 9177
 (2015). https://doi.org/10.1021/acs.jpcc.5b02561
- ¹⁸ W. A. Dunlap-Shohl, E. T. Barraza, A. Barrette, K. Gundogdu, A. D. Stiff-Roberts, and D. B. Mitzi, *ACS Energy Lett.* 3, 270 (2018). https://doi.org/10.1021/acsenergylett.7b01144
- ¹⁹ Y. Wang, X. Sun, R. Shivanna, Y. Yang, Z. Chen, Y. Guo, G. C. Wang, E. Wertz, F. Deschler, Z. Cai, and H. Zhou, *Nano Lett.* 16, 7974 (2016). https://doi.org/10.1021/acs.nanolett.6b04297
- ²⁰ M. Era, T. Hattori, T. Taira, and T. Tsutsui, *Chem. Mater.* 9, 8 (1997). https://doi.org/10.1021/cm960434m
- ²¹ L. A. Frolova, D. V. Anokhin, A. A. Piryazev, S. Y. Luchkin, N. N. Dremova, K. J. Stevenson, and P. A. Troshin, *J. Phys. Chem. Lett.* 8, 67 (2017). https://doi.org/10.1021/acs.jpclett.6b02594
- ²² Q. Ma, S. Huang, X. Wen, M. A. Green, and A. W. Ho-Baillie, *Adv. Energy Mater.* 6, 1502202 (2016). https://doi.org/10.1002/aenm.201502202
- ²³ J. Chen, Y. Fu, L. Samad, L. Dang, Y. Zhao, S. Shen, L. Guo, and S. Jin, *Nano Lett.* 17, 460 (2017). https://doi.org/10.1021/acs.nanolett.6b04450
- ²⁴ X. Mo, X. Li, G. Dai, P. He, J. Sun, H. Huang, and J. Yang, *Nanoscale* 11, 21386 (2019). https://doi.org/10.1039/c9nr06682a
- ²⁵ A. Ishteev, L. Luchnikov, D. S. Muratov, M. Voronova, A. Forde, T. Inerbaev, V. Vanyushin, D. Saranin, K. Yusupov, D. Kuznetsov, and A. Di Carlo, *Appl. Phys. Lett.* 119, 071901 (2021). https://doi.org/10.1063/5.0055993
- ²⁶ J. Li, R. Gao, F. Gao, J. Lei, H. Wang, X. Wu, J. Li, H. Liu, X. Hua, and S. F. Liu, *J. Alloys Compd.* 818, 152903 (2020). https://doi.org/10.1016/j.jallcom.2019.152903

- ²⁷ Y. Ling, L. Tan, X. Wang, Y. Zhou, Y. Xin, B. Ma, K. Hanson, and H. Gao, *J. Phys. Chem. Lett.* 8, 3266 (2017). https://doi.org/10.1021/acs.jpclett.7b01302
- ²⁸ C. Chen, T. H. Han, S. Tan, J. Xue, Y. Zhao, Y. Liu, H. Wang, W. Hu, C. Bao, M. Mazzeo, and R. Wang, *Nano Lett.* 20, 4673 (2020). https://doi.org/10.1021/acs.nanolett.0c01550
- ²⁹ J. V. Barth, G. Costantini, and K. Kern, Nature, 437(7059), pp.671-679 (2005). https://doi.org/10.1038/nature04166
- ³⁰ H. Brune, Surf. Sci. Rep. 31, 125 (1998). https://doi.org/10.1016/S0167-5729(99)80001-6
- ³¹ C. Qiu, A. Dumont, P. Li, and Z. H. Lu, *Adv. Photonics Res.* 2, 2000140 (2021). https://doi.org/10.1002/adpr.202000140
- ³² S. Cheng, Y. Lee, J. Yu, L. Yu, and M. D. Ediger, *J. Phys. Chem. Lett.* 14, 4297 (2023). https://doi.org/10.1021/acs.jpclett.3c00728
- M. Shahiduzzaman, K. Yonezawa, K. Yamamoto, T. S. Ripolles, M. Karakawa, T. Kuwabara, K. Takahashi, S. Hayase, and T. Taima, ACS Omega 2, 4464 (2017). https://doi.org/10.1021/acsomega.7b00814
- ³⁴ Y. Zhang, L. Luo, J. Hua, C. Wang, F. Huang, J. Zhong, Y. Peng, Z. Ku, and Y. B. Cheng, *Mater. Sci. Semicond. Process.* 98, 39 (2019). https://doi.org/10.1016/j.mssp.2019.03.021
- ³⁵ H. Li, G. Tong, T. Chen, H. Zhu, G. Li, Y. Chang, L. Wang, and Y. Jiang, *J. Mater. Chem.*A 6, 14255 (2018). https://doi.org/10.1039/c8ta03811b
- ³⁶ N. Chand, J. Cryst. Growth 97, 415 (1989). https://doi.org/10.1016/0022-0248(89)90223-6
- ³⁷ J. R. Chin, M. B. Frye, D. S. H. Liu, M. Hilse, I. C. Graham, J. Shallenberger, K. Wang, R. Engel-Herbert, M. Wang, Y. K. Shin, and N. Nayir, *Nanoscale* 15, 9973 (2023). https://doi.org/10.1039/d3nr00645j

- ³⁸ L. Harris and B. M. Siegel, *J. Appl. Phys.* 19, 739 (1948). https://doi.org/10.1063/1.1698199
- ³⁹ J. L. Richards, P. B. Hart, and L. M. Gallone, *J. Appl. Phys.* 34, 3418 (1963). https://doi.org/10.1063/1.1729216
- ⁴⁰ A. Kanak, O. Kopach, L. Kanak, I. Levchuk, M. Isaiev, C. J. Brabec, P. Fochuk, and Y. Khalavka, *Cryst. Growth Des.* 22, 4115 (2022). https://doi.org/10.1021/acs.cgd.1c01530
- ⁴¹ Y. El Ajjouri, F. Palazon, M. Sessolo, and H. J. Bolink, *Chem. Mater.* 30, 7423 (2018). https://doi.org/10.1021/acs.chemmater.8b03352
- ⁴² L. Nasi, D. Calestani, F. Mezzadri, F. Mariano, A. Listorti, P. Ferro, M. Mazzeo, and R. Mosca, *Front. Chem.* 8, 313 (2020). https://doi.org/10.3389/fchem.2020.00313
- ⁴³ V. I. Nefedov, *J. Electron Spectrosc. Relat. Phenom.* 25, 29 (1982). https://doi.org/10.1016/0368-2048(82)85002-0
- ⁴⁴ I. W. Drummond, in *Surface Analysis by Auger and X-Ray Photoelectron Spectroscopy*, edited by D. Briggs and J. T. Grant (IM Publications, Chichester, 2003), pp. 117–144.
- ⁴⁵ K. Hilpert, M. Miller, and A. Feltrin, "Vaporisation of CsBr and thermochemistry of the homocomplexes (CsBr)n(g), n = 2, 3, 4.". *HTMC X: 10th International IUPAC Conference on High Temperature Materials Chemistry*, Juelich, Germany (2000).
- ⁴⁶ A. Iizuka, E. Shibata, M. Sato, and T. Nakamura, *Thermochim. Acta* 622, 103 (2015). https://doi.org/10.1016/j.tca.2015.10.014
- ⁴⁷ J. Holovský, A. Peter Amalathas, L. Landová, B. Dzurňák, B. Conrad, M. Ledinský, Z. Hájková, O. Pop-Georgievski, J. Svoboda, T.C.J. Yang, and Q. Jeangros, *ACS Energy Lett.* 4, 3011 (2019). https://doi.org/10.1021/acsenergylett.9b02080

- ⁴⁸ P. Liška, T. Musálek, T. Šamořil, M. Kratochvíl, R. Matula, M. Horák, M. Nedvěd, J. Urban, J. Planer, K. Rovenská, and P. Dvořák, *J. Phys. Chem. C* 127, 12404 (2023). https://doi.org/10.1021/acs.jpcc.3c03056
- ⁴⁹ Y. Meng, C. Lan, F. Li, S. Yip, R. Wei, X. Kang, X. Bu, R. Dong, H. Zhang, and J. C. Ho, *ACS Nano* 13, 6060 (2019). https://doi.org/10.1021/acsnano.9b02379
- ⁵⁰ Y. Wang, V. Schmidt, S. Senz, and U. Gösele, *Nat. Nanotechnol.* 1, 186 (2006). https://doi.org/10.1038/nnano.2006.133
- ⁵¹ A. Rothman, K. Bukvišová, N. R. Itzhak, I. Kaplan-Ashiri, A. E. Kossoy, X. Sui, L. Novák, T. Šikola, M. Kolíbal, and E. Joselevich, *ACS Nano* 16, 18757 (2022). https://doi.org/10.1021/acsnano.2c07480
- ⁵² Y. Yang, C. Hou, and T. X. Liang, *Phys. Chem. Chem. Phys.* 23, 7145 (2021). https://doi.org/10.1039/D0CP04893C
- ⁵³ F. Bertolotti, G. Nedelcu, A. Vivani, A. Cervellino, N. Masciocchi, A. Guagliardi, and M. V. Kovalenko, *ACS Nano* 13, 14294 (2019). https://doi.org/10.1021/acsnano.9b07626
- ⁵⁴ Y. Chen, S. R. Smock, A. H. Flintgruber, F. A. Perras, R. L. Brutchey, and A. J. Rossini, *J. Am. Chem. Soc.* 142, 6117 (2020). https://doi.org/10.1021/jacs.9b13396
- ⁵⁵ V. Held, N. Mrkyvkova, Y. Halahovets, P. Nádaždy, K. Vegso, A. Vlk, M. Ledinský, M. Jergel, S. Bernstorff, J. Keckes, and F. Schreiber, *ACS Appl. Mater. Interfaces* 16, 35723 (2024). https://doi.org/10.1021/acsami.4c04095 I. V. Markov, *Crystal Growth for Beginners: Fundamentals of Nucleation, Crystal Growth and Epitaxy* (World Scientific, 2016).
- ⁵⁷ S. Liu, Y. Chen, W. Gao, W. Li, X. Yang, Z. Li, Z. Xiao, Y. Liu, and Y. Wang, *Adv. Mater.*, 35(31), p.2303544 (2023). https://doi.org/10.1002/adma.202303544